Article

The Variational Principle of a Rotor Inner-Passage Shock in the Circumferential Average Through Flow Inverse Problem of the Axial Compressors and

Tianyi Luo * , Peng Shan * , Xiaohe Yang

Posted Date: 6 April 2026

doi: 10.20944/preprints202604.0361.v1

Keywords: transonic axial flow compressor; counter-rotating fan; rotor passage shock; the variational principle of a stationed shock; momentum relaxation method; quasi-one-dimensional duct flow

Article

The Variational Principle of a Rotor Inner-Passage Shock in the Circumferential Average Through Flow Inverse Problem of the Axial Compressors and Applications †

Tianyi Luo [1], Peng Shan [2,*] and Xiaohe Yang [3]

[1] AVIC CAPDI Integration Equipment Co., Ltd., Beijing, 100120, PR China
[2] School of Energy and Power Engineering, Beihang University, Beijing, 100191, PR China
[3] AECC Commercial Aircraft Engine Co., Ltd., Shanghai, 200241, PR China
* Correspondence: PShan@buaa.edu.cn

† This manuscript is an extended version of the GTINDIA2023-117883 meeting paper published in the Proceedings of the ASME 2023 Gas Turbine India Conference, Bangalore, India, 7–8 December, 2023.

Abstract

This paper offers an application and validation case for the recently obtained variational principle of a shock stationed in a duct. The streamline curvature method for circumferentially averaged through-flow and blading design inverse problem remains fundamentally employed in current axial compressor design systems and is indispensable as the generator of multi-stage blade coordinates. However, this method inherently smooths out flow discontinuities and thus, to date, cannot provide the stage stall margin, a key performance indicator most critical in the adjustment of high-loading stages, requiring instead a time-consuming CFD validation afterward. Leveraging the variational principle for shock stationarity, this paper acquires a method to show efficiently the stage stall margin by visualizing rotor passage shock rapidly. In the general coaxial rotating relative motion, by modeling the transonic streamlines as a set of layered quasi-one-dimensional duct flows, a variational principle of the flow impulse potential energy for the stationary normal shock is derived. It is found that the factors governing the stationarity and location of the normal shock in relative motion include the variable cross-sectional area, the frictional and other on way losses, and the variable rotational radius of the duct flow. In the applications to transonic rotor cascades, the frictional and other on way losses are prescribed. First, the discontinuous entropy generation distributions along the cascades of each transonic layer are set, to consider the boundary layer, oblique shock, normal passage shock, shock-boundary layer interference, and trail edge losses. Second, with the total streamline loss fixed by the through-flow design, all shock locations possessing positional stability are determined via the variational principle for each streamline. Third, by comparing with CFD direct problem results, a dimensionless rule governing the actual entropy generation distribution along the layer cascades is established. In three sorts of axial compressor stage design cases, this method yields consistently 3D curved-surface structures of passage shock that agree well with CFD direct problem solutions, demonstrating the effectiveness and a certain applicability.

Keywords: transonic axial flow compressor; counter-rotating fan; rotor passage shock; the variational principle of a stationed shock; momentum relaxation method; quasi-one-dimensional duct flow

1. Introduction

In the design point of an axial-flow transonic compressor rotor, there exists a normal shock behind the minimum area of the blade passage with a weaker oblique shock attached to the leading edge of the blade. The normal shock in the passage plays a crucial role in determining the performance of the compressor. On one hand, the contribution of the normal shock to the work done and pressure rise on the airflow becomes increasingly significant, which even exceed 90% of the total near the blade tip. In off-design conditions, the location of the normal shock moves upstream or downstream depending on changes in rotational speed, back pressure, mass flow, and other factors [1,2]. The different locations of the normal passage shock correspond to different states of the compressor stage and determine the characteristics and stall margin of the compressor stage. On the other hand, losses associated with the shock wave system increase rapidly with increasing Mach number of the relative inflow, potentially surpassing the blade profile loss and other secondary flow losses, significantly impacting the efficiency of the blade row [3]. Therefore, in the aerodynamic design process of a transonic compressor, knowing the location of the normal passage shock and the three-dimensional (3D) curved surface shape of it to effectively control it is of paramount importance.

In 1987, using Laser Anemometry, for the first time Wood et al. [4] from NASA Lewis Research Center obtained clear images of the 3D curved shock surface within a transonic fan rotor (Figure 1). This experiment, which remains extremely challenging even today, confirmed the existence and characteristics of rotor passage shock waves. It also provided empirical data for the development of several shock loss models and the estimation of shock locations. Currently, the main approach to obtain the position and structure of shock waves in transonic compressors is through 3D Computational Fluid Dynamics (CFD) simulations. Though CFD direct problem can provide a nearly exact viscous flow field including 3D shock structure in the design phase of compressors, the construction of grids with millions of cells, with the difficulty to be orthogonal due to the mutual interaction between the leading edges of the suction and pressure surfaces, and the computational time, required typically on the order of hours or even days, remain highly laborious and time-consuming.

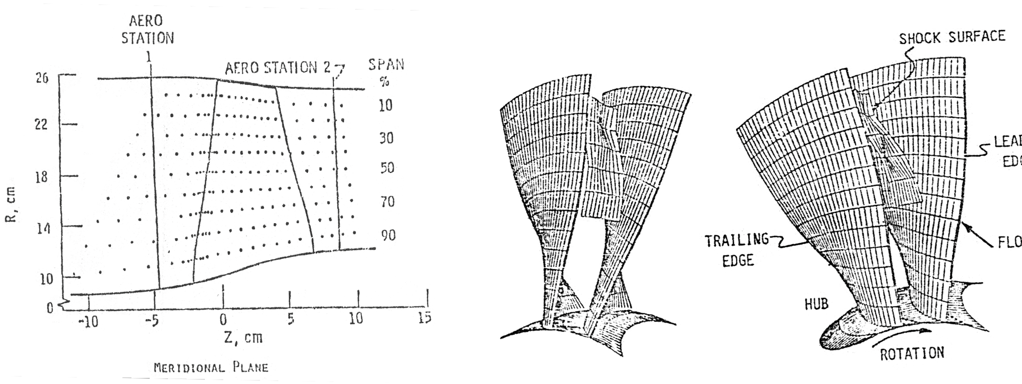

Figure 1. Earliest successfully measured rotor blade passage shock structure by using Laser Anemometry [4].

In fact, the streamline curvature method [5–7] and through-flow matrix method [8], which are representative of flow field through flow design and validation methods for turbomachinery and were developed from Wu Chung-Hua's theory of dual stream surfaces [9–13], are still highly significant in the overall aerodynamic layout process and the initial inverse and direct problems of turbomachinery, especially in multi-stage blade coordinate generations and rational optimizations, even in today's advanced CFD era. If it is possible to predict the position of the rotor passage shock and relatively evaluate the design stall margin in the through flow and blading inverse problem design phase before the use of CFD, it would provide a valuable guidance, therefore a shortened cycle and a reduced cost for the development of transonic compressors.

However, the existing through flow methods mostly smooth away the velocity abrupt transition at the shock location under the same work gain and blade row boundary conditions, without considering the actual discontinuous flow, and only using shock loss models to predict the shock losses in the blade row [14–16]. Another significant limitation is that all the existing shock loss models of axial compressor rotor focuses on studying an oblique or normal shock associated with the leading edge of the blades, rather than investigating the passage shock, which is much stronger and more influential. The classic two-dimensional (2D) shock models, represented by the M-H-L model in 1961, and the classic three-dimensional shock models, represented by the W-P model in 1982, both place the normal passage shock at the leading edge of a rotor. The kinematics of the blade leading edge curve and the leading edge oblique shock surface, developed by Peng Shan in 1996, though concerned to all oblique shocks, is also limited to those attached at the leading edge [17,18]. In recent years, there have been some emerging shock models, such as the model proposed by Banjac et al. in 2022 [19], which take into account the state of shock system under different operating conditions. These models have shown good predictive capabilities for compressor characteristics in through flow direct problems. However, the complexity of the calculations is increased due to many subdivisions in the models. On one hand, the aforementioned shock models assume an isentropic flow field everywhere except at the shock wave location, thereby neglecting the impact of losses in the upstream and downstream of the blade passage on the midstream shock wave. On the other hand, the impact of the varying quasi-radial thickness of each flow surface along the streamlines on the shock is also not considered. Since the 1980s, there have been research efforts in through flow inverse problems aimed at capturing shocks, by considering the physical nature of losses and abrupt changes in the flow field [20,21], thereby addressing the issue of flow field discontinuities in transonic compressor. However, the difficulty in computational implements has hindered their widespread adoption. Therefore, the capture of shocks in the quasi-3D design phase has not yet been achieved, the ability of shock capture like in Figure 1 is still awaited.

This paper tries to study the behavior and effects of the normal shock stationed in rotor inner-passage of axial flow compressor. The S2 mean flow surface (S2m) theory of turbomachinery is combined with the variational principle of a shock stationed in a duct [22]. By utilizing the streamlines and flow field data from the through flow inverse problem results, the spatial location and 3D curved surface of the normal passage shock are successfully solved with relatively high accuracy and efficiency. The streamline curvature method simplifies the complex 3D flow within a turbomachinery onto a quasi-3D S2m flow surface by defining S2m surface as a group of individual one-dimensional (1D) streamlines. The variational principle of a shock stationed in a duct uses the momentum relaxation method to investigate 1D or quasi-1D flow in ducts, provides a clear understanding of how parameters such as cross-sectional area variation, friction force, heat transfer, and mass addition affect, individually, the location stability of a shock in a duct. Therefore, by extending this variational principle to a rotational coordinate system, it can be applied to those quasi-1D duct flows equivalent to those supersonic streamlines but influenced by perhaps multi-parameters. Then, the momentum relaxation method can be used to solve for the locations of the normal passage shocks in each supersonic “layer cascades” of the rotor passage and analyze the location stability of each normal shock. Simultaneously, by comparing with the normal passage shock location in each layer of the rotor blade resulted from CFD, the non-dimensional distribution of the entropy generation along the layer cascades, which is introduced in the process of solving for shock locations, is adjusted to obtain the representative and widely applicable empirical data. Because of the significant impact of the normal passage shock on the performance of the compressor stage, the 3D curved shock wave formed by combining the normal passage shocks from each layer cascades allows for a relative evaluation of the adequacy of the design stall margin of the stage.

This manuscript is an extended version of the GTINDIA2023-117883 meeting paper [23]. This revised version has 1) added and explained the very essential knowledge of this engineering paper, variational principle at the static frame situation, while in the meeting paper this principle is only introduced without an elucidation; 2) integrated the area of the important Figure 3, while in the first part of this research [22], the left side of Figure 3 was tailored for the clarity of its central part, lost its fundamental nature and the utilities to be convinced and used; 3) added the CFD process descriptions for the examinations; 4) revised many descriptions for the physics comprehensions.

2. The Variational Principle of a Normal Shock Stationed in the Rotor Passage of Compressor

The streamline curvature method assumes that the flow inside a compressor is steady, compressible, adiabatic, and axisymmetric. The quasi-radial equilibrium equation, obtained by reducing Euler equations to S2m surface, combined with continuity, rothalpy conservation, entropy, and gas state equations, after being discretized, is used to solve the position and aerodynamic parameters of the streamlines on the quasi-radial computational stations distributed on S2m surface. These stations are located at the leading and trailing edges, inside and inbetween blade rows.

An excellent through flow design inverse problem combines those previous empirical models and experimental data, the resulted stage performance often corresponds well with CFD or experimental result. Therefore, it is theoretically justified to solve for the location of the normal passage shock of a rotor based on the inlet and outlet parameters of each rotor streamline given or obtained by the through flow design. Moreover, this approach is consistent with the variational principle of a shock in a duct, in which the inlet and outlet boundary conditions are fastened to ensure the duct flow is a conservative system.

2.1. The Variational Principle of a Normal Shock Stationed in the Rotor Passage of Compressor

Consider a steady, area-variable, adiabatic, non-isentropic quasi-1D duct flow in an axis-fixed rotational coordinate system, whose central streamline has a variable rotational radius r. The meridional projection of this flow is depicted in Figure 2. This quasi-1D duct flow is a flow within a relative motion frame and is influenced by three parameters: cross-sectional area, frictional and other losses, and the rotational radius. Numbers 0, 1, 2 and 3 represent respectively the sections at the duct inlet, ahead of the shock, behind the shock and at the duct outlet.

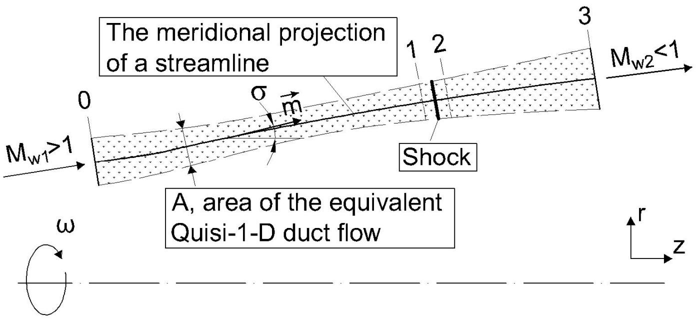

Figure 2. Meridional projection of a steady, area-variable, adiabatic, non-isentropic quasi-1D duct flow in an axis-fixed rotational coordinate system. Its central streamline has a variable rotational radius r.

Since the blade row inlet and outlet flow conditions are already solved out by the through flow problem, the shock stationed in this duct also satisfies the variational principle of a shock in a duct [22], i.e., for a control volume CV containing a shock inside a duct, the real stationary location of the shock makes the functional "the potential energy of flow impulse"

$$J = -\int_{CV} (pA + \dot{m}v)dx \tag{1}$$

integrated through the entire duct minimal, among all the potential energies integrated upon each possible location satisfying the determined inlet and outlet boundary conditions of the duct. As shown in Figure 3 in an absolute coordinate system, for the adiabatic isentropic variable-area duct, or the constant-area frictional duct, the real stationary location of the shock makes the functional "the potential energy of flow impulse" minimal. In the relative motion frame of rotor cascades, the area A in Eq. (1) should be the flow cross-sectional area A_w normal to the relative velocity w. The mass flow $\dot{m}$ should be the relative mass flow $\dot{m}_w$ in relative motion frame, while it is noted that $\dot{m}_w = \rho w A_w = \rho v A = \dot{m}$. The velocity v should be the relative velocity w. So, for terse, the subscripts are omitted and the symbols A, $\dot{m}$, w are still adopted to represent variables A_w, $\dot{m}_w$, w in relative motion frame in the text followed. Therefore it is derived that, the stationary shock must satisfy the condition that the change rate of the flow impulse ahead of the shock is smaller than that behind the shock, i.e.,

$$\frac{D(pA+\dot{m}w)_1}{dx} < \frac{D(pA+\dot{m}w)_2}{dx} \tag{2}$$

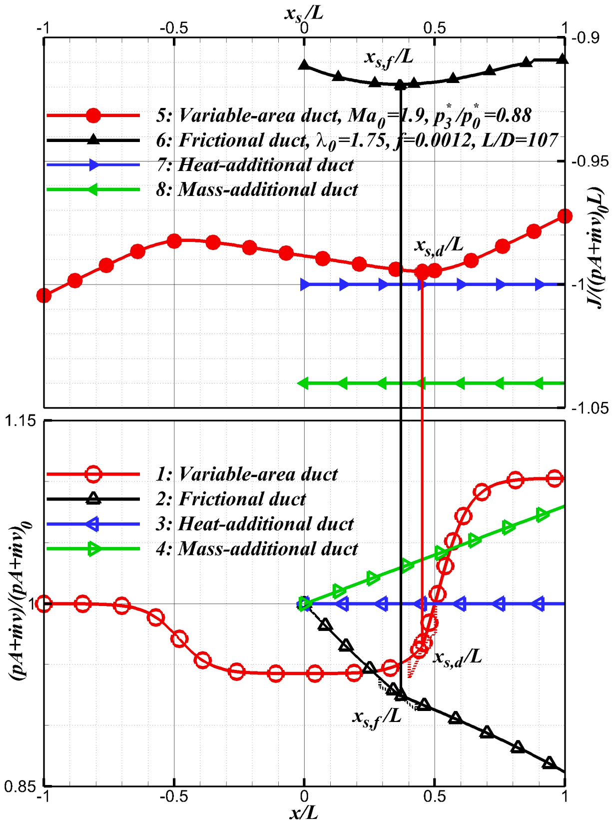

Figure 3. In an adiabatic isentropic variable-area duct, constant-area frictional duct, constant-area heat-addition duct, and constant-area mass-addition duct with inlet or throat at 0 and outlet at 1, the distribution of the dimensionless flow impulse upstream and downstream of the real dimensionless shock location $x_{s,d}/L$ or $x_{s,f}/L$, and the dimensionless potential energy J of the flow impulse for the shock stationed at all possible dimensionless shock locations x_s/L [22].

Here the operator D represents the convective differential change of a fluid particle in the relative motion frame. p, w, and $\dot{m}$ are respectively the static pressure, relative velocity, and relative mass flow of the gas in the quasi-1D duct. A is the cross-sectional area of the tube of relative velocity. x represents the distance along the instantaneous flow direction of the relative motion streamline. Subscripts 1 and 2 represent respectively the planes right ahead of and right behind the normal shock. For a steady flow, the convective derivative of an aerodynamic parameter q on S2m surface can be expressed as the following five forms

$$\frac{Dq}{Dt} = w_r\frac{\bar{\partial} q}{\partial r} + w_z\frac{\bar{\partial} q}{\partial z} = w\frac{Dq}{dx} = w_m\frac{Dq}{dm} = w_z\frac{Dq}{dz} \tag{3}$$

where m represents the meridional direction of the streamline, dm and dz represent respectively the increments in the direction m and axial coordinate z when the particle moves by dx alone the relative tube. Further, since $w_m = w cos\beta$ and $w_z = w_m cos\sigma$, it yields

$$\frac{Dq}{dz} = \frac{1}{cos\beta cos\sigma}\frac{Dq}{dx} \tag{4}$$

where β is the relative flow angle, σ is the angle between direction z and m, from z to m, w_m is the meridional relative velocity, and w_z is the axial relative velocity. Since the geometric parameters of S2m surface are already provided by the through flow solution, both angle β and angle σ are known. Those convective derivative equations in this paper can be easily transformed into derivatives referring to the axial coordinate z by Eq. (4), for more convenient calculations.

The quasi-1D relative motion duct flow obeys the mass flow equation

$$\dot{m} = \rho w A = const \tag{5}$$

the entropy equation

$$\frac{1}{\rho} Dp = -TDs + Dh \tag{6}$$

the rothalpy conservation equation along the central line of the duct, i.e., the streamline

$$I \equiv h + \frac{1}{2} w^2 - \frac{1}{2} \omega^2 r^2 = const \tag{7}$$

where ρ, T, s, h and I represent respectively the density, static temperature, entropy, static enthalpy and rothalpy per unit of mass, ω is the angular velocity of the relative motion frame.

Differentiating Eq. (7) and substituting it into Eq. (6), one obtains the momentum equation of the quasi-1D duct flow

$$\frac{1}{\rho}\frac{Dp}{dx} = -T\frac{Ds}{dx} - w\frac{Dw}{dx} + \omega^2 r\frac{Dr}{dx} \tag{8}$$

Eqs. (5), (7), (8), and the perfect gas state equation

$$p = R\rho T \tag{9}$$

form the governing equations of this quasi-1D duct flow, where R is the gas constant. Once the distributions of the cross-sectional area, rotational radius, and losses along this quasi-1D duct are known, the distributions of aerodynamic parameter such as density, pressure, and relative velocity can be determined. It is evident that the distribution of loss will be discontinuous if a shock is present in the flow.

To simplify the computation of the variational principle in this paper, the governing equations of the quasi-1D relative motion duct flow, which aligns with the rotor streamline obtained by the through flow problem, are based on the following assumptions:

1) The flow fields at the rotor inlet and outlet calculation stations of the through flow inverse problem remain unchanged.
2) Suppose that the rothalpy conservation equation still holds in the flow when losses are present.
3) All the streamlines in the rotor passage remain unchanged. It means that the direction of velocity remains the same while the magnitude of velocity w may vary. This approach preserves the radial equilibrium velocity field corresponding to the loss model in the original through flow design, without solving for a radial equilibrium velocity field upon the loss distribution model of this paper [24].

In this paper, the momentum relaxation method [22] is also employed to solve for the location of the normal shock. This involves fixing those boundary conditions at the rotor inlet and outlet, which are the mass flow, rothalpy, and entropy, then solving for the aerodynamic parameters at every points along the duct flow. According to the fact that the flow impulse ahead of the shock is equal to that behind the shock, i.e.

$$(pA + \dot{m}w)_1 = (pA + \dot{m}w)_2 \tag{10}$$

the shock location can be obtained by an iterative process. Multiplying both sides of Eq. (8) by ρA, and substituting Eq. (5) and Eq. (9) into, we obtain

$$\frac{D(pA+\dot{m}w)}{dx}=p\frac{DA}{dx}-\frac{pA}{R}\frac{Ds}{dx}+\rho A\omega^2 r\frac{Dr}{dx} \tag{11}$$

According to Eq. (11) and the variational principle Eq. (2) of a shock stationed in a duct, in this quasi-1D duct flow, the variable cross-sectional area, losses such as friction, and variable rotational radius are three factors that collectively determine the location and location stability of the shock. Their effects on the location stability are as follows:

1) Cross-sectional area, $p\frac{DA}{dx}$. Since the pressure behind the shock is always greater than that ahead of the shock, when the area of the duct increases, this term tends to make the change rate of the flow impulse behind the shock greater than that ahead of the shock, thereby to enhance the stability of the shock. And vice versa, decreases, to make the change rate smaller, to reduce.
2) Losses, $-\frac{pA}{R}\frac{Ds}{dx}$. Since the pressure behind the shock is always greater than that ahead of the shock, when the entropy generation rate behind the shock is greater than that ahead of the shock, this term tends to make the change rate of the flow impulse behind the shock smaller than that ahead of the shock, thereby to reduce the stability of the shock. And vice versa, smaller, to make the change rate greater, to enhance. The diversity and complex correlation of losses in rotor blades also make the impact of losses on the location stability of the shock complex, which will be discussed in detail in the following sections.
3) Rotational radius, $\rho A\omega^2 r\frac{Dr}{dx}$. Since the density behind the shock is always greater than that ahead of the shock, when the streamline radius increases, this term tends to make the change rate of the flow impulse behind the shock greater than that ahead of the shock, thereby to enhance the stability of the shock. And vice versa, decreases, to make the change rate smaller, to reduce.

In literatures, the study for shock position vibration and shock–surface structure stabilization are pursued primarily by analyzing the unsteady interactions of strong and weak waves, in the scene of area-variable duct [25–28]. In the steady analysis of variational principle [24], to the adiabatic isentropic area-variable duct flow, the area variation rate is the unique parameter for shock stationarity. Here the relative motion analysis of Eq. (11) notes that, when existing non-shock on-way entropy generation and rotating radius raising, the known relation between shock stationarity and variable-area for a pure area-variable duct flow may be changed.

2.2. Equivalent Conversion Between Streamline and Quasi-1D Duct Flow

The width and thickness are specified along each streamline of the through flow inverse problem to create a series of cascades, named layer cascades, shown in Figure 4. Then, a conversion from a layer cascades to an equivalent quasi-1D duct flow is performed. This equivalent duct flow has characteristics as follows:

1) The flow is a steady, area-variable, adiabatic, non-isentropic quasi-1D duct flow in a rotational frame, its central streamline has a variable rotational radius. The interactions between adjacent duct flows are completely neglected.
2) The geometry of the central streamline of the equivalent duct flow, including the rotational radius, relative flow angle, etc., is identical to that of the streamline of through flow problem. The aerodynamic parameters of the equivalent duct flow to be solved are parameters on its

central streamline, and are identified also as the uniform parameters alone the normal line within S1 surface of the through flow streamline.

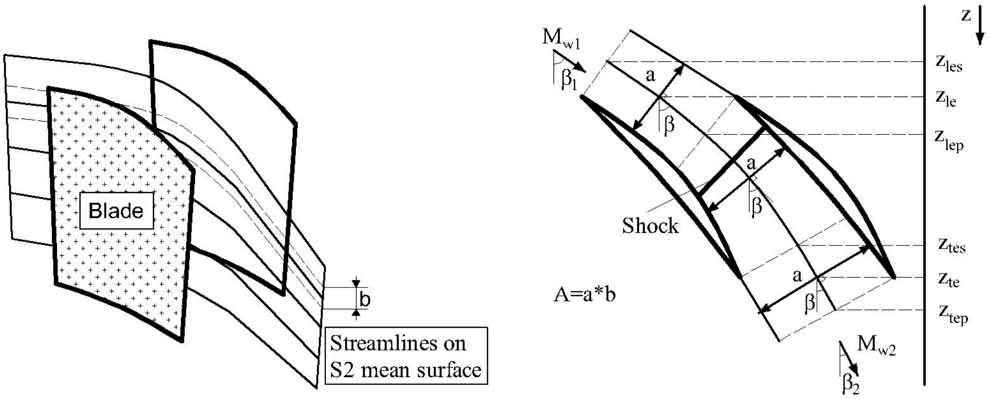

Figure 4. Illustration of the width a and thickness b of the layer cascades for the equivalent quasi-1D duct flow.

3) The distribution of the cross-sectional area A of the relative motion equivalent quasi-1D duct flow is defined here. The meridional projection m of the streamline is adopted as the independent variable. Taking the aerodynamic parameter values on the through flow streamline as that of the duct flow, by the dispensed mass flow $\dot{m}$ of the duct, one determines

$$A = \frac{\dot{m}}{n_b \rho' w'} \tag{12}$$

where n_b is the total number of blades, ρ' and w' are the density and relative velocity along the through flow streamline. The width of the layer cascades, i.e., the S1 surface width a at a point of the through flow streamline is defined as first, the length of the normal line, which passes that point, extends from its intersection point with the blade suction surface to its intersection point with the blade pressure surface. Then, the width a takes the shortened length minus the aerodynamic wall blockage thickness. The thickness b of the layer cascades is obtained by $A = a \times b$.

4) The inlet of the equivalent duct flow is positioned at the location z_{les} where the perpendicular line from the central streamline intersects the leading edge of the suction surface. The outlet is positioned at the location z_{tep} where the perpendicular line from the central streamline intersects the trailing edge of the pressure surface. The area and entropy of the equivalent duct flow at the inlet and outlet are equal to that obtained from the through flow problem at those locations, respectively.

5) In the equivalent duct flow, 100-200 computational nodes are set between z_{les} and z_{tep}, while the through flow problem typically takes single figures of calculation stations in a blade row. Therefore the equivalent duct flow should interpolate the geometric and aerodynamic parameters from the yielded through flow streamlines, such as the rotational radius, flow angle, cross-sectional area, and so on.

6) To modify the cross-sectional area of the duct flow, a layer thickness expansion factor ϕ can be introduced, where the modified area is $(1+\phi)A$. This modification serves two purposes. First, it helps prevent a severe choking of the streamlines near the leading edge where the flow Mach number $M_{w,le}$ is close to 1 during the subsequent calculations using the momentum relaxation method. Second, it corrects for the increase in layer thickness caused by complex flow

phenomena such as tip leakage flow and endwall boundary layer in real flows, which can result in deflection of the streamlines. To ensure that the inlet and outlet areas of the equivalent duct flow match the through flow results, the layer thickness expansion factor is set to zero at the inlet position z_{les} and gradually increases to its maximum value at the minimum area location of the equivalent duct flow. It then decreases to zero at the outlet location z_{tep} on the pressure surface. The maximum value of the layer thickness expansion factor can be set to a value less than 0.005, as it does not significantly affect the stationary location of the shock.

7) In this paper, the mass flow of each layer cascades takes

$$\dot{m}_j = \frac{\dot{m}_{total}}{n} \tag{13}$$

where $\dot{m}_{total}$ is the total mass flow of the compressor, n is the total number of streamlines in the through flow problem, and the subscript j denotes the streamline identifier. The flow ratio $\dot{m}_r$ of streamline j is defined as the ratio of the mass flow between the streamline 1 and streamline j to the total mass flow.

3. The Losses in a Compressor Passage and the Distribution of Losses

The distribution of losses in the rotor passage is one of the determining factors of the shock location. On one hand, the flow in the rotor passage is highly complex, and the losses resulting from various flow conditions have not been fully elucidated. On the other hand, in the through flow inverse problem of transonic axial stage, losses are often lumped together and smoothly distributed along the streamlines. The momentum relaxation method in this paper is based on the through flow design results and requires a rotor passage loss distribution model different from both approaches mentioned above. This model can capture the main factors influencing the shock location without overly complicating the loss calculation process.

The loss distribution model for the rotor layer cascades presented here does not change the total loss magnitude calculated in the through-flow inverse problem using the rotor D-factor model. Then, the total loss is decomposed into five parts: boundary layer loss for the entire passage, leading edge oblique shock loss, passage shock loss, shock boundary layer interaction loss, and wake loss. These losses were estimated based on classical empirical models and distributed in appropriate passage position. In the early stages of this research, Seddon's [29] model for intake shock boundary layer interference loss was used to estimate the interference loss, then it was distributed after the shock position. Based on Schlichting's [30] study, the entropy generation due to wake loss was set as 15% to 22% of the total entropy generation along the streamlines and distributed after the trailing edge. Unfortunately, the constructed loss distribution models were difficult to obtain shock location solutions that approximated CFD results, and the numerical convergence was poor. Therefore, the amplification factors for these losses were introduced into the calculations, and the layer thickness expansion factor was also introduced during this process. Additionally, various loss distribution types were considered and tested. Taking the advantage of spent only a few times, in the order of seconds, for computing the momentum relaxation method incorporating loss distribution models, the problem was quickly resolved by continuously adjusting the magnitudes of these factors on different streamlines. By summarizing the patterns observed in these numerical experiments, the final loss distribution model was obtained.

The total losses inside the duct are comprised of boundary layer loss, shock losses, and other losses, i.e.

$$\Delta s_{total} = \Delta s_b + \Delta s_s + \Delta s_o \tag{14}$$

where Δs_{total} is the total entropy generation. The entropy generation Δs_b caused by the boundary layer exists throughout the entire duct. Δs_s is the local entropy generation directly caused by oblique and normal shocks. The other entropy generation $\varDelta s_o$ encompasses the entropy generation caused by shock boundary layer interference loss, trailing edge loss, etc., which is distributed downstream of the normal passage shock.

3.1. Boundary Layer Loss

According to the boundary layer entropy generation model studied by Denton[3] for turbomachinery, the total entropy generation caused by the boundary layer from the upstream of a certain point x to this point in the cascades is given by

$$S = \int_0^x \frac{\rho v_\delta^3 C_d}{T_\delta} dx \tag{15}$$

where v_δ and T_δ represent respectively the velocity and temperature at the edge of the boundary layer, corresponding respectively to relative velocity w and relative total temperature T_R^* in this paper. C_d is the dimensionless loss coefficient. For many blade rows in turbomachinery with a boundary layer momentum thickness Reynolds number Re_θ on the order of 1000, Denton & Cumpsty [31] suggest that C_d can be approximated as a constant value of 0.002. The relative total temperature is

$$T_R^* = \frac{\left(h + \frac{1}{2} w^2\right)}{c_p} \tag{16}$$

where c_p is the specific heat at constant pressure. Substituting Eqs. (5), (7), and (16) into Eq. (15) and taking the partial derivative with respect to the 3D relative streamline x, the change rate of the entropy generation per unit mass caused by the boundary layer along the equivalent duct flow is obtained as

$$\frac{Ds_b}{dx} = c_p \frac{C_d w^2}{\left(H + \frac{1}{2} \omega^2 r^2\right) a} \tag{17}$$

According to Eqs. (15) and (17), in the loss distribution algorithm, the specific entropy generation caused by the boundary layer at each point can be integrated using the aerodynamic parameter values of current iteration and gradually converges during the iteration.

3.2. Leading Edge Oblique Shock Loss and Normal Passage Shock Loss

The shock loss $\varDelta s_s$ consists of the leading edge oblique shock loss $\varDelta s_{s,o}$ and the normal passage shock loss $\varDelta s_{s,n}$. Besides being solved by the plane shock formula, when solving for the shock location by using the momentum relaxation method, the normal passage shock loss is obtained by subtracting the boundary layer loss, oblique shock loss, and other losses from the total loss of the through flow inverse problem.

In the study by Boyer et al. [32], the oblique shock Mach number was obtained by using the M-H-L shock model. Then, the average shock angle was replaced with the shock angle that the velocity behind the shock is exactly at the speed of sound. Finally, the oblique shock loss is calculated using oblique shock formula. The oblique shock entropy generation obtained by this method is denoted here as $\varDelta s'_{s,o}$. This estimating method tends to be accurate when the leading edge relative Mach number $M_{w,le} < 1.3$, but to be overestimated at higher Mach number, and the deviation becomes larger as the relative Mach number increases. There are two main factors contributing to this issue. First, as the leading edge Mach number increases, the portion of the oblique shock behind which the Mach number is greater than 1 becomes larger. Therefore, the average shock angle becomes smaller compared to the shock angle that leads to an exactly speed of sound behind the shock. Second, the decrease in the average shock angle makes the oblique shock more likely to intersect with the normal shock. As a result, the flow fraction passing through the oblique shock decreases. Based on these considerations, the oblique shock entropy generation obtained from this method is corrected in this study. The corrected method is

$$\Delta s_{s,o} = \Delta s'_{s,o} / M_{w,le}^2 \tag{18}$$

The oblique shock loss by this correction is linearly distributed and reaches $\Delta s_{s,o}$ in front of the normal passage shock.

3.3. Other Losses and the After Shock Entropy Generation Ratio

Other losses Δs_o can be obtained by subtracting the boundary layer loss Δs_{brs} downstream of the normal shock from the total losses Δs_{as} of the duct flow downstream of the normal shock, i.e.

$$\Delta s_o = \Delta s_{as} - \Delta s_{brs} \tag{19}$$

Account for the rapid increase of losses caused by shock boundary layer interference and furtherly the rapid increase of losses due to the mixing in the wake after trailing edge, distributing Δs_o in a quadratic manner in the rear of the normal shock is reasonable, i.e., the other losses $\Delta s_{o,z}$ at a certain position z is

$$\Delta s_{o,z} = \frac{(z - z_s)^2}{\left(z_{tep} - z_s\right)^2} \Delta s_o \tag{20}$$

where z_s is the z coordinate of the shock location. Meanwhile, a quadratic distribution also enhances the convergence of the computational program. The losses after the normal shock can be directly expressed as a fraction of the total losses Δs_{tot} along the through flow streamline, i.e.

$$\Delta s_{as} = \psi \Delta s_{tot} \tag{21}$$

where ψ is a ratio that represents the proportion of the entropy generation in the rear of the shock relative to the total entropy generation across the cascades, referred to as the after shock entropy generation ratio.

This part of the losses is the most complex component of the rotor passage losses. Not only in real flow field but also in numerical computation, the rotor is a duct flow driven by two parameters: a generalized friction including all kinds of losses and a variable cross-sectional area, simultaneously the two parameters interact nonlinearly, making the duct flow solution increasingly challenging. Therefore, the parameter after shock entropy generation ratio ψ is introduced. For any given shock location, a corresponding after shock entropy generation ratio is there. So this approach fully corresponds to the physical mechanism of the area-variable and frictional two-parameter duct flow, and marks the occurrence point of large-scale separation loss by the shock location. This makes the loss calculation complexity bypassed and the loss equations closed. Then, this approach is applied to various types of transonic axial compressor rotors. By combining it with the results of CFD direct problem, the regularities of the after shock entropy generation ratio are summarized. The specifics are as follows.

First, the oblique shock loss $\Delta s_{s,o}$ is obtained from Eq. (18), and the boundary layer loss Δs_{bfs} in front of the shock is obtained from Eq. (15). Then, using the governing equations of equivalent quasi-1D duct flow, namely Eq. (5) and Eqs. (7) to (9), the flow parameters in front of the normal shock are numerically solved to obtain the Mach number ahead of the normal shock. Further the loss $\Delta s_{s,n}$ of the normal shock is calculated by the plane shock formula. Finally, the losses of the duct flow after the normal shock is yielded as

$$\Delta s_{as} = \Delta s_{tot} - \Delta s_{s,o} - \Delta s_{bfs} - \Delta s_{s,n} \tag{22}$$

and the ratio ψ is given by Eq. (21).

Subsequently, the boundary layer loss Δs_{brs} in the rear of the normal shock and the flow parameters in the rear of the normal shock are determined. Till now, all the aerodynamic parameters and geometric parameters of the flow are known. By using Eq. (11), the change rates of the flow impulse ahead of and behind the normal shock can be solved. Combined with Eq. (2), the stability of this shock location can be analyzed.

In addition, two constraints need to be imposed. First, the shock position z_s is limited to be between the through flow leading edge location z_{le} and the suction surface trailing edge location z_{tes} of the through flow problem, i.e., $z_{le} \leq z_s \leq z_{tes}$. Second, the sum of other losses, including the shock boundary layer interference loss and wake loss and so on, should be greater than 15% of the total streamline losses. Thus combining Eqs. (19) and (21), it has

$$\psi > 15\% + \frac{\Delta s_{brs}}{\Delta s_{tot}} \tag{23}$$

By following the above mentioned steps, all the locations where the normal passage shock in each supersonic layer cascades of the rotor can be stationary are obtained. Fortunately, for rotor blades obtained by well designed through flow inverse problem, the real normal passage shock locations resulted from CFD direct problem, are all included among all possible stationary locations of the normal shock obtained by the variational principle program with these steps. The pattern of the after shock entropy generation ratio ψ corresponding to the real shock location in CFD result is what we are looking for.

For any assumed location z_s of the normal shock based on the pattern of the after shock entropy generation ratio ψ, the loss distribution of the equivalent flow is calculated using the aforementioned distribution model of losses. The governing equations of the equivalent flow is then solved for the parameter distributions of the upstream and downstream flows separately. Due to the momentum equations ahead of and behind the assumed shock location are relaxed, the two flow impulses on shock surfaces may not be equal. Therefore, whether the assumed location is the real stationary location of the normal shock or not needs to be judged by the momentum relaxation method, such as Eq. (10), and the variational principle Eq. (2).

4. Numerical Validation

According to the models presented in Sections 2.1 to 3.3, and building upon the design results of the S2m streamline curvature through flow and blading inverse problem of an axial compressor, a variational principle program for rotor passage shock stationarity was developed using FORTRAN language. This program includes the variational principle program to solve all possible shock stationary positions and the momentum relaxation method program to solve the shock stationary location. To validate the practicality of the method and obtain the pattern of the after shock entropy generation ratio ψ, the proposed method was applied to many transonic axial compressor rotors, which belong to different types. Three of the most representative cases are presented here, they are the first rotor of a five-stage compression system, the front rotor of a high-pressure-ratio counter-rotating fan, and the rear rotor of a civil low-pressure-ratio counter-rotating fan. These compressors were designed by Xiaohe Yang between 2008 and 2010 [33,34].

The 3D steady viscous flow fields of the three stages were simulated employing the commercially available CFD software FINE™ Turbo by NUMECA International. The governing equations are Reynolds averaged Navier-Stokes equations, solved with a finite volume method. Turbulence closure is achieved using one-equation Spalart-Allmaras turbulence model. The spatial discretization scheme is a central difference scheme with 2nd and 4th order artificial viscosity. Time integration is based on an explicit four-stage Runge-Kutta scheme. Implicit residual smoothing, variable time steps, and three-level multigrid are used to accelerate convergence. The inlet boundary condition consists of the inlet total pressure, total temperature, circumferential and radial airflow angles. Static pressure is given at the outlet. All wall boundary conditions were modelled as no-slip and adiabatic. The HOH-type topology structure grid is employed for both contra-stages. 69 points are set in the span-wise direction. Nine grid cells of Butterfly-type topology structure are set within the tip clearance in the span-wise direction. The total grid point numbers are 682,464 and 629,832 for the front- and aft-rotor of the civil contra-stage respectively, while they are 658,075 and 653,723 for that of the high-pressure contra-stage. The grid points near the wall are refined to impose $y^+ < 2$. Considering the special aerodynamic characteristics of the contra-stage, the grid independence of numerical simulation using NUMECA software was verified. When 1.6 times as many grid points as present are used and simulated again with the same topology structure and boundary conditions, the discrepancy of results is less than 0.157%.

The curved shock surfaces in these CFD cases are determined by analyzing the static pressure distributions in the flow field of each layer cascades.

4.1. First Rotor of a Dual-channel Five-Stage Compression System

A dual-channel five-stage compression system, which is designed through compression system overall layout design and five-stage integrative through flow design, consists of two fan stages, two compressor stages, and one high pressure centrifugal stage. The meridional flowpath and blade rows are shown in Figure 5. The aerodynamic design parameters are listed in Table 1. The corrected performance curves at 100% rotating speed are shown in Figure 6, they demonstrate the aerodynamic characteristics and the rationality of design parameters of the compression system.

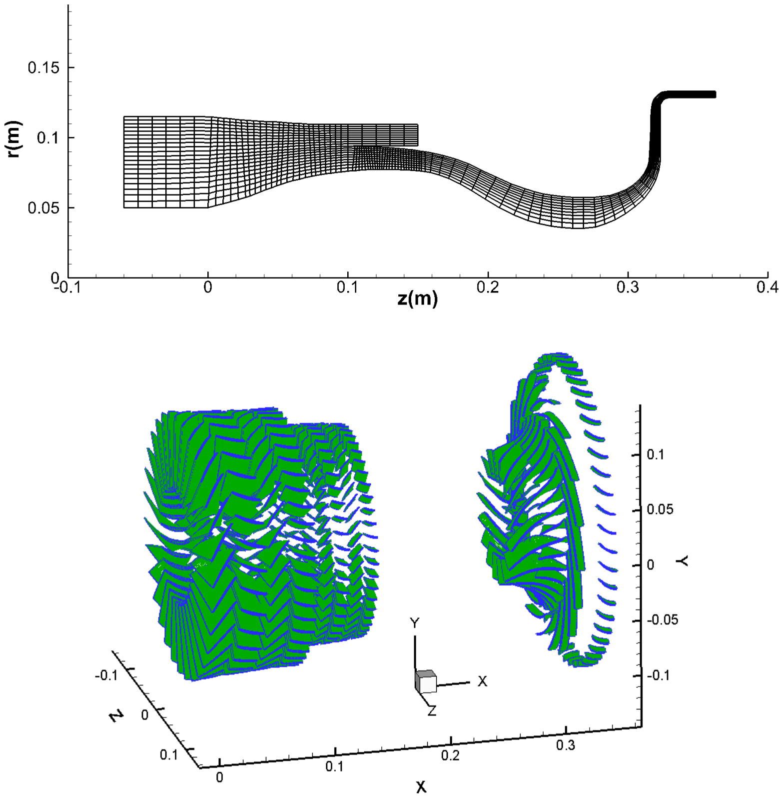

Figure 5. Meridional flowpath and 11-row bladings of a dual-channel five-stage compression system.

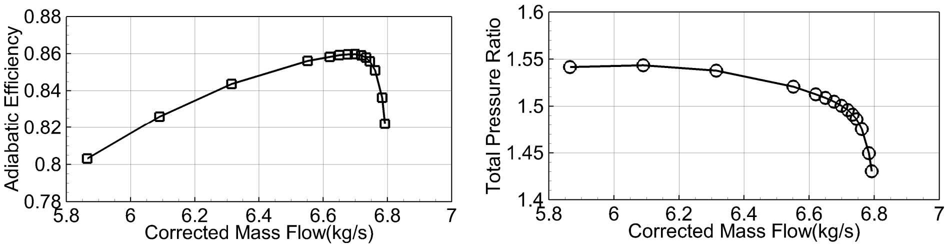

Figure 6. Corrected performance curves of the first fan stage at 100% rotating speed in a dual-channel five-stage compression system.

Table 1. Aerodynamic design parameters of a dual-channel five-stage combined compression system.

Fan mass flow $\frac{kg}{s}$	6.80
Inner channel mass flow $\frac{kg}{s}$	3.14
Bypass ratio	1.166
Inner channel total pressure ratio	12.00
Bypass channel pressure ratio	2.23
Low pressure shaft rotating speed rpm	31910
High pressure shaft rotating speed $/rpm$	62910
Tip speed of the first fan $\frac{m}{s}$	384
Pressure ratio of the first fan	1.500
Adiabatic efficiency of the first fan	0.860
CFD surge margin of the first fan	17%

Figure 7 shows, by the solid black lines, the after shock entropy generation ratio ψ for all possible stationary locations of the normal shock of each supersonic layer cascades obtained by the variational principle program at the design point of the first rotor of five-stage compression system. The ψ for the normal shock locations obtained by CFD are represented by triangle symbols. The ψ finally adopted by the momentum relaxation method are represented by the solid red lines with solid circles. The vertical axis here represents the relative blade span of the inlet rotational radius r_0 of each supersonic layer cascades, while the total blade span is the difference between the inlet rotational radius r_{tip0} at the tip layer cascades and the inlet rotational radius r_{hub0} at the hub layer cascades. It can be observed that the range of the ψ for all possible stationary locations of the normal shock near the blade tip is relatively narrow, while the range widens towards the blade root. The ψ for the normal shock locations obtained by CFD are all around the maximum values of the ψ for all possible stationary locations of the normal shock. The former is almost the same as the later near the blade tip, while the former becomes much smaller than the later towards the blade root.

Figure 8 presents, by the thin solid black lines, the cross-sectional area ratio A/A_{tip0} alone each equivalent duct flow of the layer cascades of the first rotor of five-stage compression system at the design point; by the thick solid blue lines with small solid circles, the area ratio for all possible stationary locations of the normal shock in each supersonic layer cascades; by the dashed red line with hollowed circles, the area ratio for the normal shock locations of CFD; by the solid red line with solid circles, the area ratio for the normal shock locations of the momentum relaxation method; by the dashed black lines with upward and downward triangles, the area ratio at the locations of the leading edge z_{lep} on the pressure surface and the trailing edge z_{tes} on the suction surface of each layer cascades, respectively. Here the horizontal axis represents the axial coordinate z at a certain point in the layer cascades relative to the positions of the inlet z_{le} and outlet z_{te} in the through flow problem. The vertical axis represents the cross-sectional area A at that point relative to the cross-sectional area A_{tip0} at the inlet of the layer cascades at the blade tip. It is noted that, the positions of the minimum cross-sectional areas of each supersonic layer cascades, i.e., the throat positions, approach the blade leading edge gradually from the blade tip to the blade root. The throat positions near the blade tip are between the pressure surface leading edge point z_{lep} and the suction surface trailing edge point z_{tes}. The stationary locations of the normal passage shocks are all near the throat positions.

doi:10.20944/preprints202604.0361.v1

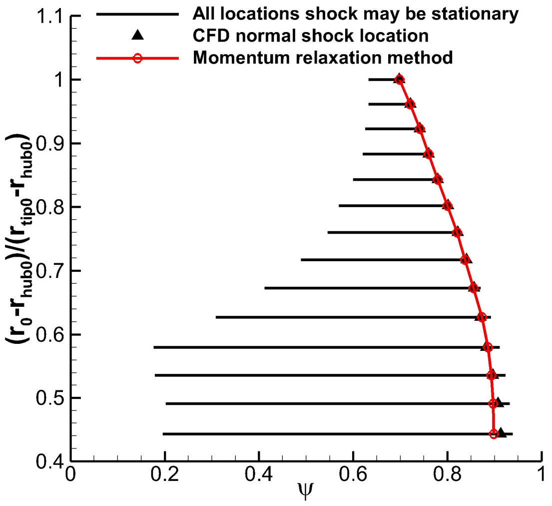

Figure 7. After shock entropy generation ratio ψ for all possible stationary locations of the normal shock of each supersonic layer cascades obtained by the variational principle program at the design point of the first rotor of five-stage compression system, ψ for the normal shock locations obtained by CFD, and ψ finally adopted by the momentum relaxation method.

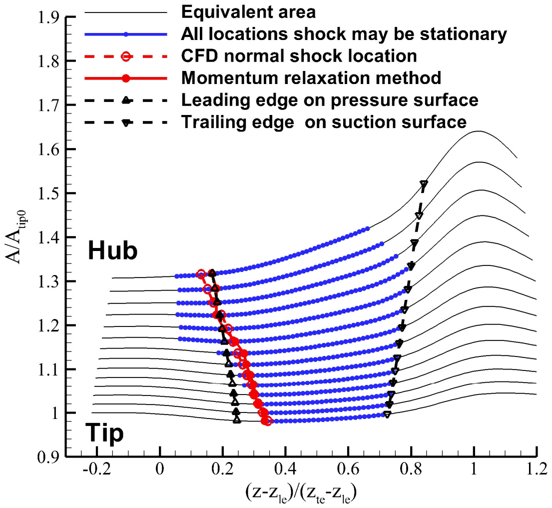

Figure 8. Cross-sectional area ratio, for alone each equivalent duct flow of the layer cascades of the first rotor of five-stage compression system at the design point; for all possible stationary locations of the normal shock in each supersonic layer cascades; for the normal shock locations of CFD; for the normal shock locations of the momentum relaxation method.

Figure 9 presents the 3D curved surface structure of the normal passage shock obtained respectively by the momentum relaxation method and CFD for the first rotor of five-stage compression system at the design point. It is observed that the normal passage shock of the CFD result approaches the blade leading edge gradually from the blade tip to the blade root and merges with the leading edge oblique shock at approximately 75% blade span. The surface structure of the normal passage shock obtained by the momentum relaxation method is in good agreement with that of the CFD result.

Figure 10 shows the after shock entropy generation ratio ψ of all possible stationary locations of the normal shock obtained by the variational principle program within the layer cascades at the blade spans respectively with 80%, 90%, and 100% flow ratio of the first rotor of five-stage compression system.

Figure 11 presents the chordwise distributions of entropy s and relative Mach number M_w within the layer cascades at the blade span with 90% flow ratio of that rotor, which are obtained respectively by the through flow problem, momentum relaxation method, and CFD, while CFD results are circumferentially averaged data. The entropy and Mach number distributions by the through flow problem and CFD are both circumferentially averaged, and it is seen that both methods correspond well at the inlet and outlet of the cascades, that is why the supersonic through flow inverse problem still achieves successful designs although the discontinuities are smoothed out. The distributions obtained by the momentum relaxation method are the results uniform along the normal direction of the central streamline within the layer cascade, showing the presence of discontinuities, the contrastive magnitudes of the local entropy generation of the normal shock, and of the entropy generation of the upstream and downstream ducts, and the real distribution of Mach numbers.

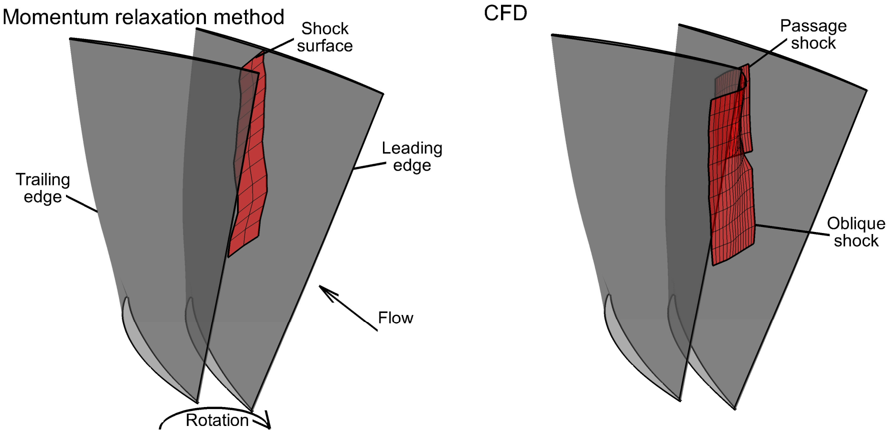

Figure 9. 3D curved surface structure of the normal passage shock obtained respectively by the momentum relaxation method and CFD for the first rotor of five-stage compression system at the design point.

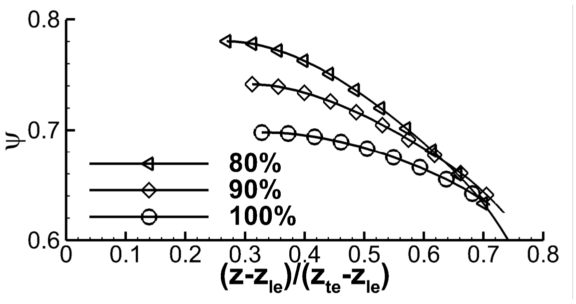

Figure 10. After shock entropy generation ratio ψ of all possible stationary locations of the normal shock obtained by the variational principle program within the layer cascades at the blade spans respectively with 80%, 90%, and 100% flow ratio of the first rotor of five-stage compression system.

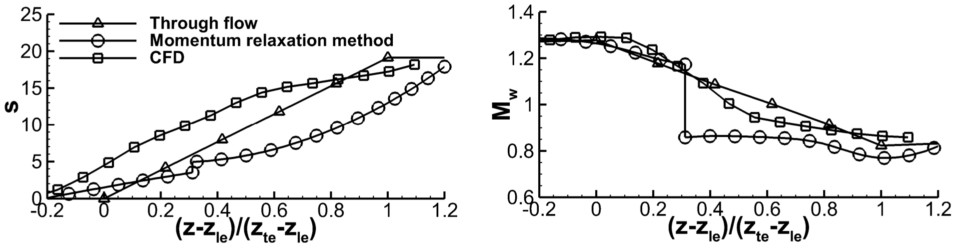

Figure 11. Chordwise distributions of entropy s and relative Mach number M_w within the layer cascades at the blade span with 90% flow ratio of the first rotor of five-stage compression system, obtained respectively by the through flow problem, momentum relaxation method, and CFD.

doi:10.20944/preprints202604.0361.v1

Figure 12 shows the contour plots of the relative Mach number for the S1 surface within the layer cascades at the blade span with 90% flow ratio of that rotor, which are obtained by the momentum relaxation method (up) and CFD (down). This layer cascades is located at approximately 92% blade span, to compare the fundamental differences between the two methods, the CFD simulation does not include tip clearance. The momentum relaxation method fails to capture the flow acceleration caused by the expansion wave around the leading edge of the suction surface, as a result, the Mach number ahead of the normal shock is lower, but it is generally similar to the Mach number in front of the normal shock near the pressure surface. The Mach number behind the normal shock obtained by momentum relaxation method is around 0.86, which is slightly lower than 0.9 obtained by CFD.

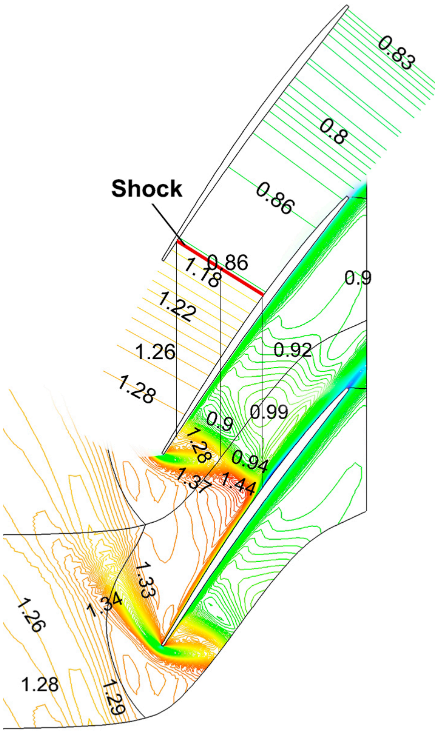

Figure 12. Contour plots of the relative Mach number for the S1 surface within the layer cascades at the blade span with 90% flow ratio of the first rotor of five-stage compression system, which are obtained by the momentum relaxation method (up) and CFD (down).

4.2. Front Rotor of a High-Pressure-Ratio Counter-Rotating Fan Stage

The meridional flowpath and blade rows of a high-pressure-ratio counter-rotating fan stage are shown in Figure 13. The aerodynamic design parameters are listed in Table 2. The corrected performance curves are shown in Figure 14.

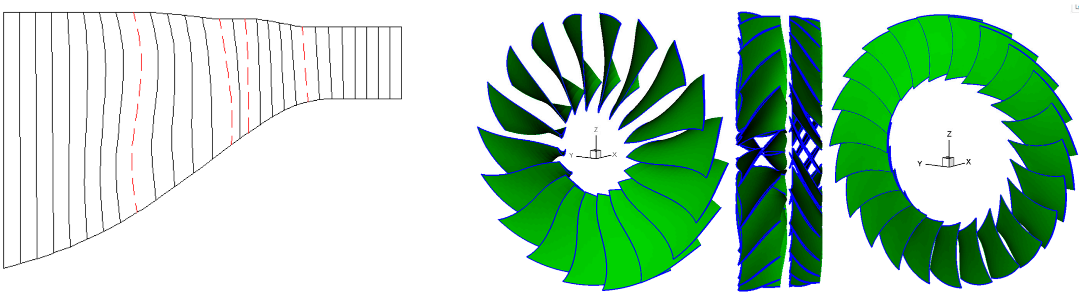

Figure 13. Meridional flowpath and bladings of a high-pressure-ratio counter-rotating fan stage.

Table 2. Aerodynamic design parameters of a high-pressure-ratio counter-rotating fan stage.

	Front	Rear
Tip speed $\frac{m}{s}$	500	-391
Pressure ratio	2.170	1.613
Mass flow per frontal area $kg/(s,m^2)$	184.9	-
Mass flow per annulus area $kg/(s,m^2)$	203.1	-
Mass flow coefficient at mean-radius	0.535	-
Work coefficient L_u/U_{Tip}^2	0.322	0.422
Reaction of the rotor	0.682	1.323
Hub-tip ratio	0.300	0.596
Diffusion factor D at mean-radius	0.506	0.414
Hub relative Mach	0.754	1.534
Tip relative Mach	1.636	1.593
Blade count	18	21
Average solidity	1.970	1.856
Aspect ratio	1.746	1.536
Reaction of the stage	0.379	
Pressure ratio of the stage	3.496	
Adiabatic efficiency of the stage	83.8%	
CFD surge margin of the stage	14%	

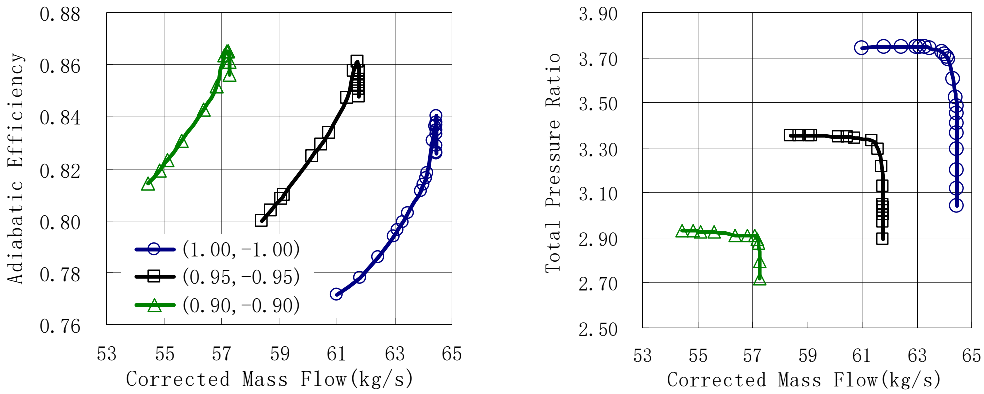

Figure 14. Corrected performance curves of a high-pressure-ratio counter-rotating fan stage.

Figure 15 shows the after shock entropy generation ratio ψ for all possible stationary locations of the normal shock of each supersonic layer cascades obtained by the variational principle program at the design point of the front rotor of the high-pressure-ratio counter-rotating fan stage, ψ for the normal shock locations obtained by CFD, and ψ finally adopted by the momentum relaxation method. The ψ for all possible stationary locations of the normal shock and the spanwise distribution pattern of the ψ of the normal shock locations obtained by CFD here are similar to Figure 7.

Figure 16 presents the cross-sectional area ratio A/A_{tip0} alone each equivalent duct flow of the layer cascades of the front rotor of the high-pressure-ratio counter-rotating fan stage at the design point, the area ratio for all possible stationary locations of the normal shock in each supersonic layer cascades, the area ratio for the normal shock locations of CFD, the area ratio for the normal shock locations of the momentum relaxation method, the area ratio at the locations of the leading edge z_{lep} on the pressure surface and the trailing edge z_{tes} on the suction surface of each layer cascades, respectively. It is noted that, the positions of the minimum cross-sectional areas of each supersonic layer cascades, i.e., the throat positions, approach the blade leading edge gradually from the blade tip to the blade root. The throat positions near the blade tip are between the pressure surface leading edge point z_{lep} and the suction surface trailing edge point z_{tes}. The stationary locations of the normal passage shocks are all near the throat positions.

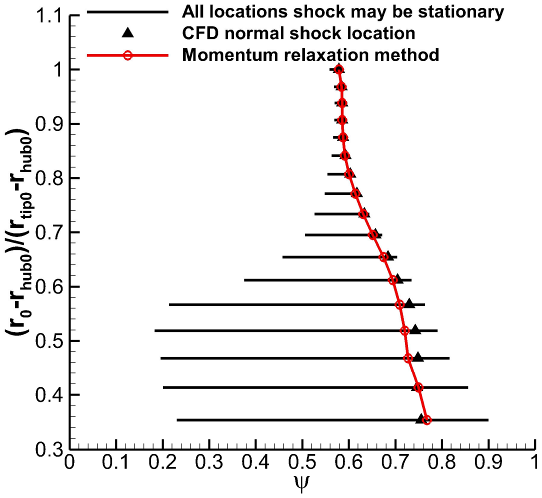

Figure 15. After shock entropy generation ratio ψ for all possible stationary locations of the normal shock of each supersonic layer cascades obtained by the variational principle program at the design point of the front rotor of the high-pressure-ratio counter-rotating fan stage, ψ for the normal shock locations obtained by CFD, and ψ finally adopted by the momentum relaxation method.

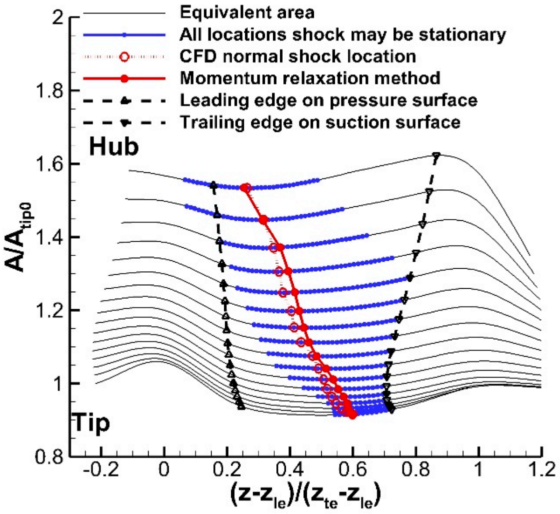

Figure 16. Cross-sectional area ratio, for alone each equivalent duct flow of the layer cascades in the front rotor of the high-pressure-ratio counter-rotating fan stage at the design point; for all possible stationary locations of the normal shock in each supersonic layer cascades; for the normal shock locations of CFD; for the normal shock locations of the momentum relaxation method.

Figure 17 presents the 3D curved surface structure of the normal passage shock obtained respectively by the momentum relaxation method and CFD for the front rotor of the high-pressure-ratio counter-rotating fan stage at the design point. It is observed that the normal passage shock of the CFD result approaches the blade leading edge gradually from the blade tip to the blade root, but the shock system is always a dual-shock system, consisting of a leading-edge oblique shock and a passage normal shock. The surface structure of the normal passage shock obtained by the momentum relaxation method is in good agreement with that of the CFD result.

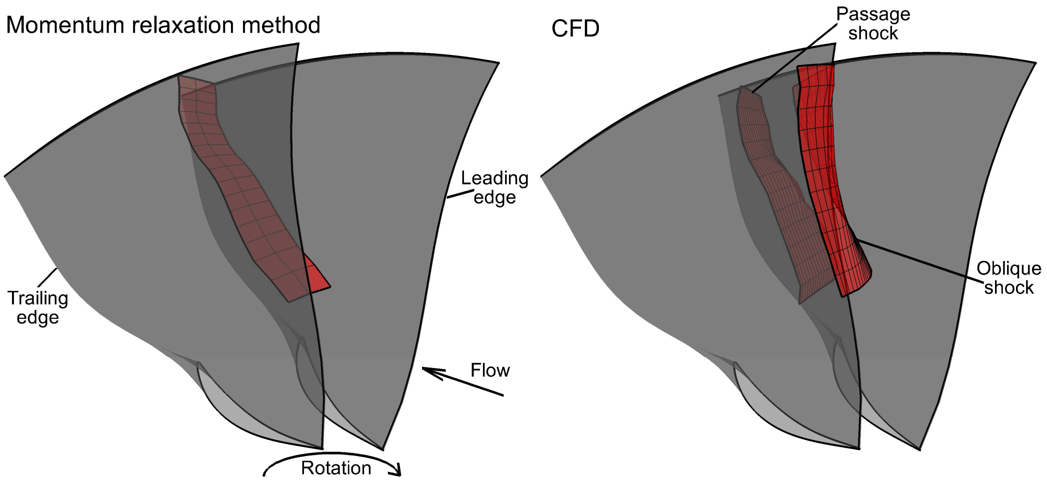

Figure 17. 3D curved surface structure of the normal passage shock obtained respectively by the momentum relaxation method and CFD for the front rotor of the high-pressure-ratio counter-rotating fan stage at the design point.

Figure 18 shows the after shock entropy generation ratio ψ of all possible stationary locations of the normal shock obtained by the variational principle program within the layer cascades at the blade spans respectively with 80%, 90%, and 100% flow ratio of the front rotor of the high-pressure-ratio counter-rotating fan stage.

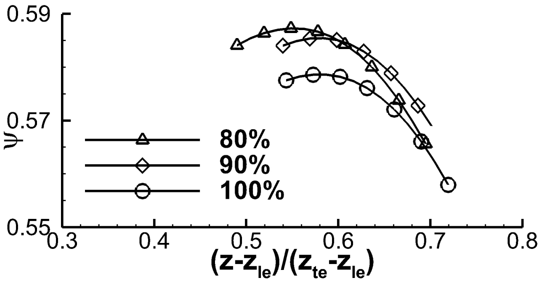

Figure 18. After shock entropy generation ratio ψ of all possible stationary locations of the normal shock obtained by the variational principle program within the layer cascades at the blade spans respectively with 80%, 90%, and 100% flow ratio of the front rotor of the high-pressure-ratio counter-rotating fan stage.

Figure 19 presents the chordwise distributions of entropy s and relative Mach number M_w within the layer cascades at the blade span with 90% flow ratio of that rotor, which are obtained respectively by the through flow problem, momentum relaxation method, and CFD, while CFD results are circumferentially averaged data.

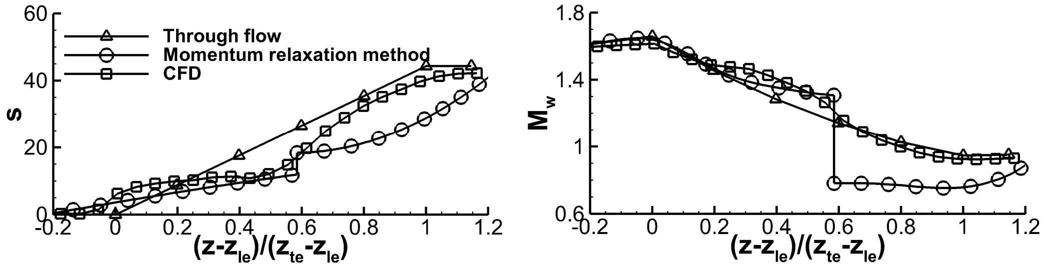

Figure 19. Chordwise distributions of entropy s and relative Mach number M_w within the layer cascades at the blade span with 90% flow ratio of the front rotor of the high-pressure-ratio counter-rotating fan stage, obtained respectively by the through flow problem, momentum relaxation method, and CFD.

doi:10.20944/preprints202604.0361.v1

When the stationary location of the normal shock moves backward from the leading edge, the boundary layer loss in front of the shock will increase. If, in this situation, the Mach number ahead of the shock decreases, resulting in a reduced normal shock loss, it may increase the after shock entropy generation ratio. As the stationary location of the normal shock continuously moves backward and the Mach number ahead of the shock increases, the normal shock loss increase, inevitably leading to a decrease in the after shock entropy generation ratio relative to the total losses resulted from the through flow problem. Therefore, in this case, the layer cascades near the blade tip show the situation that, as the stationary location of the shock moves backward, the after shock entropy generation ratio initially increases and then decreases. Similar situations can also be observed in the case of the first rotor of the dual-channel five-stage compression system, as shown in Figure 10. It is found that in the layer cascades near the blade tip, the real location of the normal passage shock is always the possible stationary location that maximizes the after shock entropy generation ratio ψ to its maximum value ψ_{max}, and in the layer cascades closer more to the blade root, the ψ of the real location of the normal shock deviates from the maximum value ψ_{max} more. Therefore, in Figure 7 and Figure 15, when using the momentum relaxation method to determine the location of the normal passage shock, to estimate the after shock entropy generation ratio ψ, it takes an empirical formula

$$\psi = \begin{cases} \psi_{max} & \dot{m}_r \geq 0.75 \\ \left(1 - \dfrac{0.75 - \dot{m}_r}{12} \cdot \dfrac{M_{w,le} - M_{wt}}{M_{wb} - M_{wt}}\right) \psi_{max} & \dot{m}_r < 0.75 \end{cases} \tag{24}$$

where ψ_{max} belongs to the concerned layer cascades such as in Figure 15, obtained by the variational principle program. M_{wt} is the leading edge Mach number of the blade tip, and M_{wb} is the leading edge Mach number of the layer cascades with 75% flow ratio. Both are obtained from the through flow inverse problem.

Figure 20 shows the contour plots of the relative Mach number for the S1 surface within the layer cascades at the blade span with 90% flow ratio of that rotor, which are obtained by the momentum relaxation method (up) and CFD (down). This layer cascades is located at approximately 94% blade span, the CFD simulation includes tip clearance. The expansion wave around the leading edge of the suction surface causes an increase in Mach number, then the Mach number decreases after passing through the oblique shock. The strong normal passage shock does not cause boundary layer separation on the suction surface. Due to the influence of tip leakage flow, a large low velocity region is formed near the pressure surface in the rear of the normal shock. The Mach number ahead of the normal shock obtained from the momentum relaxation method is similar to the Mach number ahead of the normal shock near the pressure surface in the CFD result, and the variation trends of the distribution of the Mach number along the layer cascades and the elementary cascades are also generally consistent.

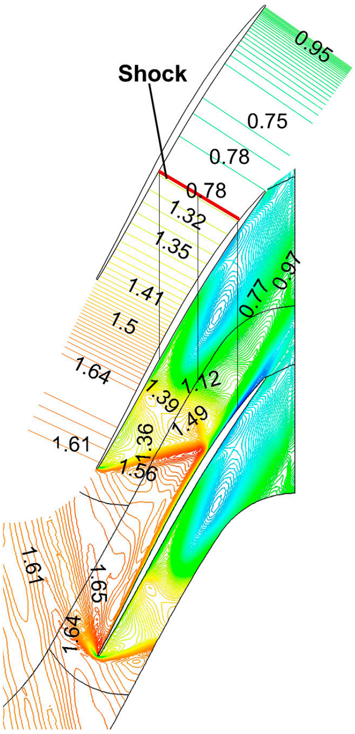

Figure 20. Contour plots of the relative Mach number for the S1 surface within the layer cascades at the blade span with 90% flow ratio of the front rotor of the high-pressure-ratio counter-rotating fan stage, which are obtained by the momentum relaxation method (up) and CFD (down).

4.3. Rear Rotor of a Civil Low-Pressure-Ratio Counter-Rotating Fan Stage

The meridional flowpath and blade rows of a civil low-pressure-ratio counter-rotating fan stage are shown in Figure 21. The aerodynamic design parameters are listed in Table 3. The corrected performance curves are shown in Figure 22.

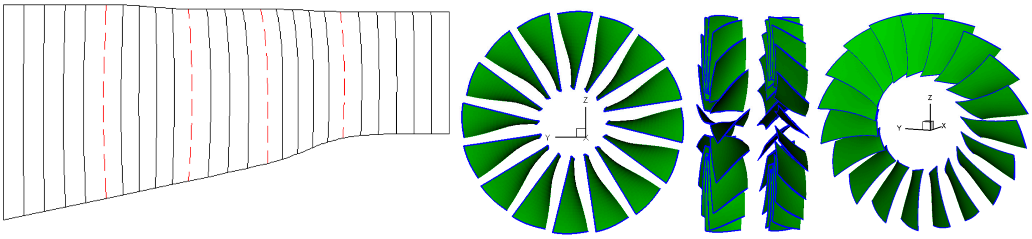

Figure 21. Meridional flowpath and bladings of a civil low-pressure-ratio counter-rotating fan stage.

Table 3. Aerodynamic design parameters of a civil low-pressure-ratio counter-rotating fan stage.

	Front	**Rear**
Tip speed $\frac{m}{s}$	300	-222
Pressure ratio	1.328	1.205
Mass flow per frontal area $kg/(s,m^2)$	200.9	-
Mass flow per annulus area $kg/(s,m^2)$	220.8	-
Mass flow coefficient at mean-radius	1.029	-
Work coefficient L_u/U_{Tip}^2	0.289	0.396
Reaction of the rotor	0.911	1.489
Hub-tip ratio	0.300	0.433

doi:10.20944/preprints202604.0361.v1

Diffusion factor D at mean-radius	0.417	0.351
Hub relative Mach	0.681	0.892
Tip relative Mach	1.165	1.219
Blade count	16	19
Average solidity	1.290	1.581
Aspect ratio	2.216	1.851
Reaction of the stage	0.521	
Pressure ratio of the stage	1.608	
Adiabatic efficiency of the stage	91.2%	
CFD surge margin of the stage	18.9%	

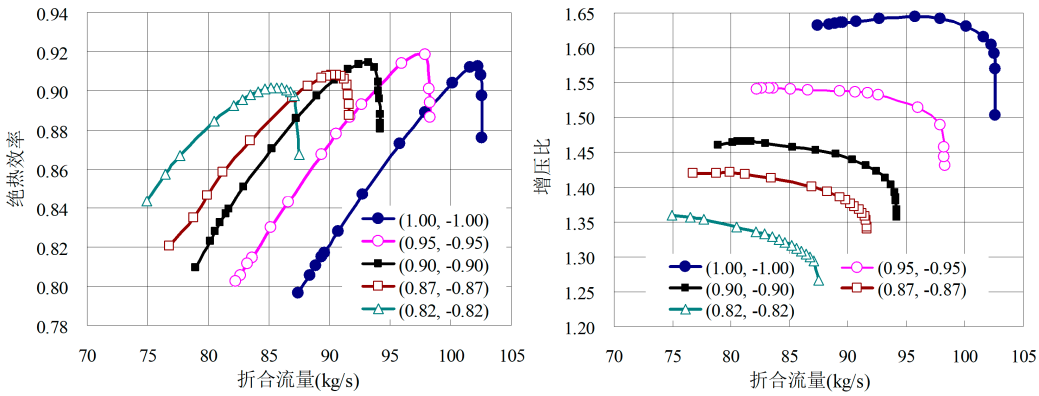

Figure 22. Corrected performance curves of a civil low-pressure-ratio counter-rotating fan stage.

Figure 23 shows the after shock entropy generation ratio ψ for all possible stationary locations of the normal shock of each supersonic layer cascades obtained by the variational principle program at the design point of the rear rotor of the low-pressure-ratio counter-rotating fan stage, ψ for the normal shock locations obtained by CFD, and ψ finally adopted by the momentum relaxation method. The ψ for all possible stationary locations of the normal shock and the spanwise distribution pattern of the ψ of the normal shock locations obtained by CFD here are similar to Figure 7 . For a change, the difference between the maximum values of the ψ for all possible stationary locations of the normal shock and the ψ of the normal shock locations obtained by CFD is always substantial along the spanwise direction.

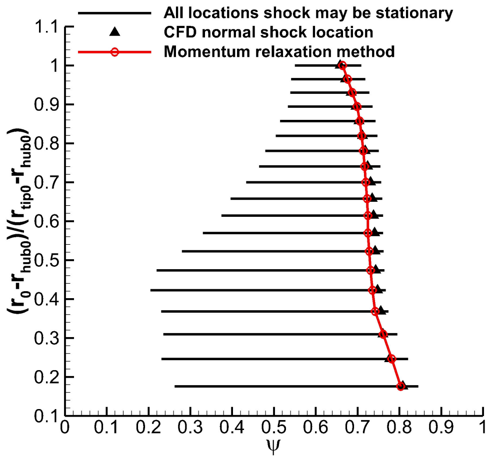

Figure 23. After shock entropy generation ratio ψ for all possible stationary locations of the normal shock of each supersonic layer cascades obtained by the variational principle program at the design point of the rear rotor

of the low-pressure-ratio counter-rotating fan stage, ψ for the normal shock locations obtained by CFD, and ψ finally adopted by the momentum relaxation method.

Figure 24 presents the cross-sectional area ratio A/A_{tip0} alone each equivalent duct flow of the layer cascades of the rear rotor of the low-pressure-ratio counter-rotating fan stage at the design point, the area ratio for all possible stationary locations of the normal shock in each supersonic layer cascades, the area ratio for the normal shock locations of CFD, the area ratio for the normal shock locations of the momentum relaxation method, the area ratio at the locations of the leading edge z_{lep} on the pressure surface and the trailing edge z_{tes} on the suction surface of each layer cascades, respectively. It is noted that, the positions of the minimum cross-sectional areas of each supersonic layer cascades, i.e., the throat positions, are all in front of the pressure surface leading edge point z_{lep}. Most of the stationary locations of the normal passage shocks are in rear of the pressure surface leading edge point z_{lep}, and gradually approach the blade leading edge from the blade tip to the blade root, and eventually surpass the blade leading edge.

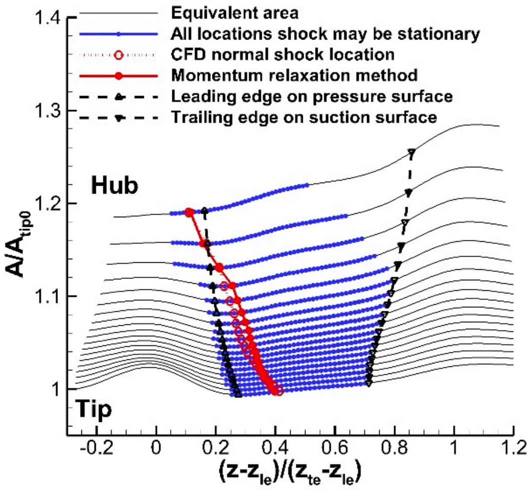

Figure 24. Cross-sectional area ratio, for alone each equivalent duct flow of the layer cascades in the rear rotor of the low-pressure-ratio counter-rotating fan stage at the design point; for all possible stationary locations of the normal shock in each supersonic layer cascades; for the normal shock locations of CFD; for the normal shock locations of the momentum relaxation method.

Figure 25 presents the 3D curved surface structure of the normal passage shock obtained respectively by the momentum relaxation method and CFD for the rear rotor of the low-pressure-ratio counter-rotating fan stage at the design point. It is observed that the normal passage shock of the CFD result approaches the blade leading edge gradually from the blade tip to the blade root, and merges with the leading edge oblique shock at approximately 70% blade span. The surface structure of the normal passage shock obtained by the momentum relaxation method is in good agreement with that of the CFD result.

Figure 26 shows the after shock entropy generation ratio ψ of all possible stationary locations of the normal shock obtained by the variational principle program within the layer cascades at the blade spans respectively with 80%, 90%, and 100% flow ratio of the rear rotor of the low-pressure-ratio counter-rotating fan stage.

Figure 27 presents the chordwise distributions of entropy s and relative Mach number M_w within the layer cascades at the blade span with 90% flow ratio of that rotor, which are obtained respectively by the through flow problem, momentum relaxation method, and CFD, while CFD results are circumferentially averaged data. In such cases, the throat of the supersonic layer cascades near the blade tip is located in front of the pressure surface leading edge point z_{lep}. Therefore, as the stationary location of the normal shock moves backward, the Mach number ahead of the shock increases, resulting in an increased normal shock loss, inevitably leading to a decrease in the after shock entropy generation ratio. Therefore, in Figure 23, when using the momentum relaxation method to determine the location of the normal passage shock, to estimate the after shock entropy generation ratio ψ, it takes an empirical formula

$$\psi = 0.95\psi_{max} \tag{25}$$

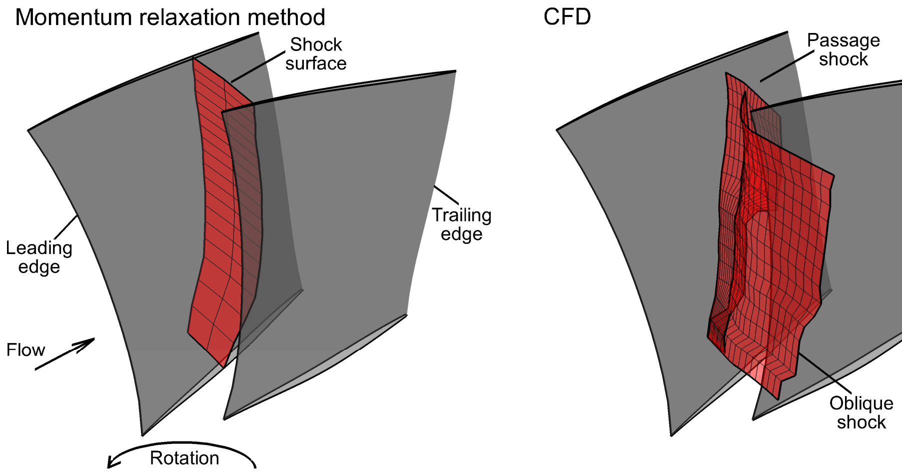

Figure 25. 3D curved surface structure of the normal passage shock obtained respectively by the momentum relaxation method and CFD for the rear rotor of the low-pressure-ratio counter-rotating fan stage at the design point.

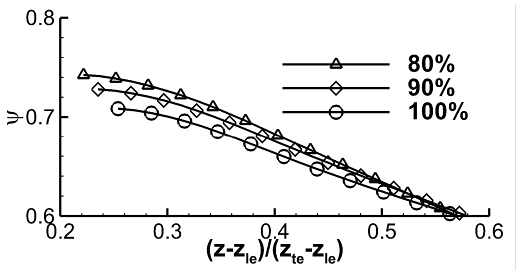

Figure 26. After shock entropy generation ratio ψ of all possible stationary locations of the normal shock obtained by the variational principle program within the layer cascades at the blade spans respectively with 80%, 90%, and 100% flow ratio of the rear rotor of the low-pressure-ratio counter-rotating fan stage.

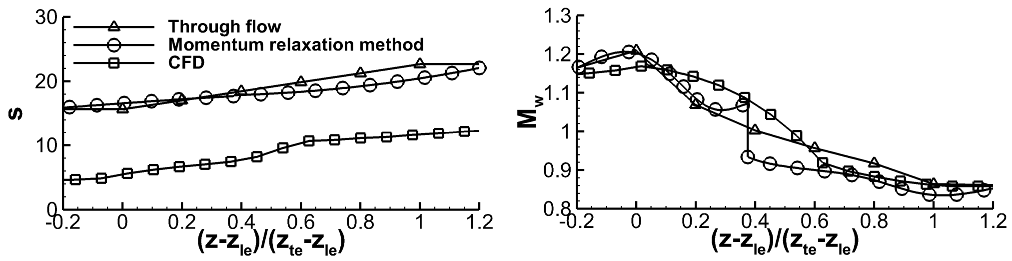

Figure 27. Chordwise distributions of entropy s and relative Mach number M_w within the layer cascades at the blade span with 90% flow ratio of the rear rotor of the low-pressure-ratio counter-rotating fan stage, obtained respectively by the through flow problem, momentum relaxation method, and CFD.

Figure 28 shows the contour plots of the relative Mach number for the S1 surface within the layer cascades at the blade span with 90% flow ratio of that rotor, which are obtained by the momentum relaxation method (up) and CFD (down). This layer cascades is located at approximately 93% blade span, the CFD simulation includes tip clearance. The expansion wave around the leading edge of the

doi:10.20944/preprints202604.0361.v1

suction surface causes an increase in Mach number, then the Mach number decreases after passing through the oblique shock. The Mach number ahead of the normal shock obtained from the momentum relaxation method is similar to the Mach number ahead of the normal shock near the pressure surface in the CFD result, and the variation trends of the distribution of the Mach number along the layer cascades and the elementary cascades are also generally consistent.

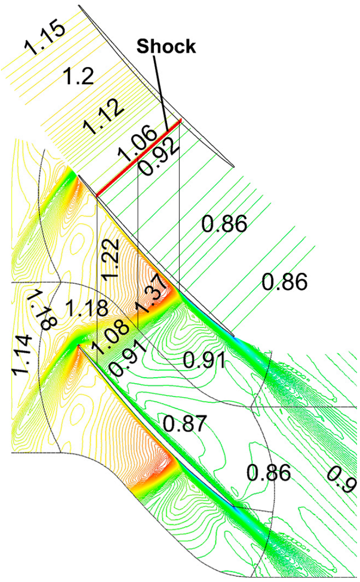

Figure 28. Contour plots of the relative Mach number for the S1 surface within the layer cascades at the blade span with 90% flow ratio of the rear rotor of the low-pressure-ratio counter-rotating fan stage, which are obtained by the momentum relaxation method (up) and CFD (down).

5. Result Analysis

Figure 29 shows the spanwise distributions of the change rate of the flow impulse ahead of and behind the normal passage shock for the three mentioned cases, where the horizontal axis is the derivation of the impulse along the axial coordinate z. It can be observed that the change rate of the flow impulse ahead of the shock is smaller than that behind the shock for each supersonic layer cascades in all cases, satisfying the variational principle of a shock stationed in a duct, i.e., Eq. (2). It should be noted that the loss caused by oblique shock is linearly distributed in front of the normal shock, which reduces the change rate of the flow impulse ahead of the normal shock according to Eq. (11). On the other hand, other losses are distributed quadratically in the rear of the normal shock and do not affect the change rate of the flow impulse right behind the normal shock. This configuration corresponds to the objective structure of a dual-shock system, where the mechanism is that the oblique shock loss, acting as the loss upstream of the normal passage shock, enhances the stationary stability of the normal passage shock.

Table 4 compares the difference between the maximum and minimum values of the after shock entropy generation ratio ψ for all possible stationary locations of the normal shocks in the layer cascades near the blade tip, specifically at the blade span with 80%, 90%, and 100% flow ratio, with the stage CFD surge margin, for the three cases. It is evident that this difference is positively correlated with the surge margin of the stage. For some poorly designed rotors, certain layer cascades may lack possible stationary locations of shocks. Although these rotors can achieve the converged flow field results through CFD, the passage shocks near the blade tip are often squeezed towards the leading edge and converged with the oblique shock, unable to form a dual-shock system structure, resulting in poor performance.

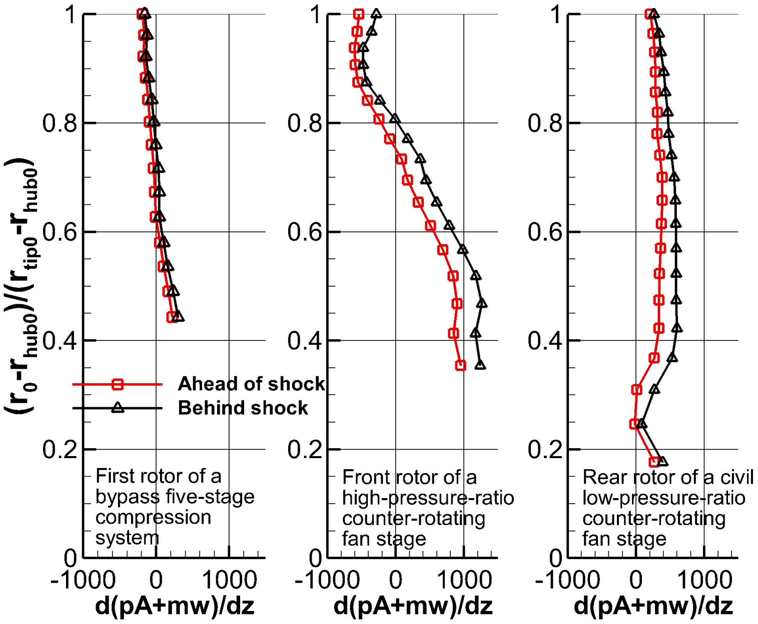

Figure 29. Spanwise distributions of the change rate of the flow impulse ahead of and behind the normal passage shock located by the momentum relaxation method for the three mentioned cases.

Table 1. **Table 4.** Comparison of the difference between the maximum and minimum values of the after shock entropy generation ratio ψ for all possible stationary locations of the normal shocks in the layer cascades near the blade tip with the stage CFD surge margin, for the three cases.

	Stage CFD surge margin	Difference between the maximum and minimum values of the after shock entropy generation ratio		
		Span with 80% flow ratio	Span with 90% flow ratio	Span with 100% flow ratio
First stage of a dual-channel five-stage com-pression system	17%	0.116	0.089	0.066
High-pressure-ratio counter-rotating fan stage	14%	0.017	0.016	0.021
Low-pressure-ratio counter-rotating fan stage	18.9%	0.21	0.177	0.159

In these three cases, the real locations of the normal passage shock are all included among all possible stationary locations of the normal shock obtained by the variational principle program. The after shock entropy generation ratios for real shock locations are all close to the maximum after shock entropy generation ratio for all possible stationary locations of the shock. For the cases that the throat positions of the layer cascades are in the rear of the pressure surface leading edge point z_{lep}, Eq. (24) can be used to obtain the after shock entropy generation ratio when solving the locations of the normal passage shocks by the momentum relaxation method. For the cases in front of the point z_{lep}, Eq. (25) can be used to obtain the after shock entropy generation ratio. The 3D curved surface structures of the normal passage shocks obtained by the momentum relaxation method are consistently in good agreement with that of the CFD result. Taking the location of the normal shock, which plays a crucial role in the stage performance, as a characterized approximate parameter, one can relatively evaluate the design stall margin of a transonic stage. This can be particularly efficient in a design-comparison-improvement process within an identical or similar design.

doi:10.20944/preprints202604.0361.v1

6. Conclusions

1) In the general coaxial rotating relative motion, by modeling the truth interrupted flow of transonic streamlines as a set of layered quasi-one-dimensional duct flows, a variational principle of the flow impulse potential energy for the stationary normal shock is derived. The shock stabilizes at the location of minimum relative potential energy.
2) Within transonic layer cascades, given the known total rotor loss, a novel discontinuous along-path entropy generation distribution has been introduced to capture the effects of boundary layers, oblique shocks, normal shocks, shock–boundary layer interactions, and wakes. An "after-shock entropy generation ratio" has been defined to concisely represent the complex flow losses downstream of the normal shock. Through comparison with CFD direct problem results, a dimensionless rule for the actual entropy generation distribution along transonic layer cascades has been established. The momentum relaxation method incorporates this rule, then undergoes the examination of variational principle. These enable the determination of the stationary location of individual normal shock, then reconstruct 3D curved-surface structure of the passage shock.
3) This work provides a practical methodology which, during the through-flow and blading design inverse problem phase of high-loading axial compressors, can predict the location and 3D shape of the passage shock with ten seconds, and enables an approximate characterization and relative evaluation whether the stall margin is sufficiently designed.

Author Contributions: Conceptualization, P.S.; methodology, T.L. and P.S.; software, T.L. and X.Y.; validation, T.L.; formal analysis, T.L.; investigation, T.L.; resources, P.S.; data curation, T.L. P.S. and X.Y.; writing—original draft preparation, T.L.; writing—review and editing, T.L and P.S.; visualization, T.L.; supervision, P.S.; project administration, P.S.; funding acquisition, P.S. All authors have read and agreed to the published version of the manuscript.

Data Availability Statement: The data presented in this study are available on request from the corresponding author.

Conflicts of Interest: The authors declare no conflicts of interest.

References

1. Wisler, D. C. Shock Wave and Flow Velocity Measurements in a High Speed Fan Rotor Using the Laser Velocimeter. *ASME J. Eng. Power*, **1977**, 99(2), 181-187.
2. Kerrebrock, J. L. Flow in Transonic Compressors. *AIAA J.* **1981**, 19, 4-19.
3. Denton, J. D., Loss Mechanisms in Turbomachines. ASME Paper No. 93-GT-435, **1993**.
4. Wood, J. R.; Strazisar, A. J.; Simanyi P. S. Shock Structure Measured in a Transonic Fan Using Laser Anemometry. Technical Report No. AGARD-CP-401, NASA-Lewis, 1987.
5. Smith, L. H. Jr. The Radial-Equilibrium Equation of Turbomachines. *ASME J. Eng. Power* **1966**, 88, pp 1-12.
6. Novak, R. A. Streamline Curvature Computing Procedures for Fluid-Flow Problem. *ASME J. Eng. Power* **1967**, 89, pp 478-490.
7. Denton, J. D. Throughflow Calculations for Transonic Axial Flow Turbines. *ASME J. Eng. Power* **1978**, 100, pp 212-218.
8. Marsh, H. A digital Computer Program for the Through-Flow Fluid Mechanics in an Arbitrary Turbomachine using a Matrix Method. *ARC R&M 3509* **1968**.
9. Wu Chung-Hua. A General Through-Flow Theory of Fluid Flow with Subsonic or Supersonic Velocity in Turbomachines of Arbitrary Hub and Casing Shapes. Paper No. NACA-TN-2302, 1951.
10. Wu Chung-Hua. A General Theory of Three-Dimensional Flow in Subsonic and Supersonic Turbomachines of Axial-, Radical-, and Mixed- Flow Type. Paper No. NACA-TN-2604, 1952.

11. Johnsen, I. A.; Bullock, R. O. Aerodynamic Design of Axial Flow Compressors. NASA SP-36, 1965.
12. Wennerstrom, A. J.; Derose, R. D.; Law, C. H. Investigation of a 1500 ft/sec, Transonic, High-Through-Flow, Single-Stage Axial-Flow Compressor with Low Hub/Tip Ratio. Technical Report No. AFAPL-TR-76-59, Aerospace Research Laboratories, Wright-Patterson Air Force Base, Ohio USA, 1976.
13. Wennerstrom, A. J. Low Aspect Ratio Axial Flow Compressor: Why and What It Means. *ASME J. Turbomach.* 111(4), **1989**, 357-365.
14. Miller, G. R.; Lewis, G. W., Jr.; Hartmann, M. J. Shock Losses in Transonic Blade Rows. *ASME J. Eng. Power* **1961**, 83, 235-241.
15. Puterbaugh, S. L.; Wennerstrom, A. J. Revision of the Shock Loss Re-Estimation Procedure of Program UD0300 Utilizing a Three-Dimensional Shock Model. Technical Report No. AFWAL-TR-82-2079. 1982
16. Wennerstrom, A. J.; Puterbaugh, S. L. A Three-Dimensional Model for the Prediction of Shock Losses in Compressor Blade Rows. *ASME J. Eng. Gas Turbines Power.* **1984**, 106(2), 295-299.
17. Shan, P. Kinematic Problems of Leading Edge Supersonic Sweep-Bend in Supersonic and Transonic Axial Compressors. Ph.D. thesis, Beijing University of Aeronautics and Astronautics, Beijing, China, 1996.
18. Shan, P. Kinematic Analysis of 3-D Swept Shock Surfaces in Axial Flow Compressors. *ASME J. Turbomach.* **2001**, 123(3), 490-500.
19. Banjac, M.; Savanovic, T.; Petkovic D.; Petrovic, M. V. A Comprehensive Analytical Shock Loss Model for Axial Compressor Cascades. *ASME J. Turbomach.* **2022**, 144(9), 091003.
20. Xu, J.; Jiang, Z.; Yang, J.; Zhang, Y.; Du, Z. An Aerothermodynamic Analysis of Transonic Compressor Rotors Containing Three-Dimensional Shocks. *ASME. J. Eng. Power.* **1982**,104(2), 386-393.
21. Sayari, N.; Bolcs, A. A New Throughflow Approach for Transonic Axial Compressor Stage Analysis. ASME Paper No. 95-GT-195, **1995**.
22. Luo, T. Y.; Shan, P. Variational principle of a shock stationed in a duct. *Phys. Fluids* **2022**, 34(5), 056102.
23. Luo, T. Y.; Shan, P.; Yang X. H. The Variational Principle of a Rotor Passage Shock in the Circumferential Average Through Flow Inverse Problem of the Axial Compressors and Applications. In Proceedings of the ASME 2023 Gas Turbine India Conference, Bangalore, India, 7-8 December 2023.
24. Epstein, A. H.; Kerrebrock, J. L.; Thompkins, W. T. Shock Structure in Transonic Compressor Rotors. *AIAA J.*, **1979**, 17(4), 79-4043.
25. Culick, F. E. C.; Rogers, T. The Response of Normal Shocks in Diffusers. *AIAA J.*, **1983**, 21(10), 1381–1390.
26. Lee, B. Self-sustained Shock Oscillations on Airfoils at Transonic Speeds. *Prog. Aerospace Sci*, **2001**, 37(2), 147-196.
27. Bur, R.; Benay, R.; Galli, A.; et al. Experimental and Numerical Study of Forced Shock-wave Oscillations in a Transonic Channel. *Aerospace Sci. Tech.*, **2006**, 10, 265–278.
28. Bruce, P. J. K.; Babinsky, H. Unsteady Shock Wave Dynamics. J. Fluid Mech. **2008**, 603, 463–473.
29. Seddon, J.; Goldsmith, E. L. *Intake aerodynamics*. American Institute of Aeronautics and Astronautics, New York, 1985.
30. Schlichting, H. *Boundary layer theory*, 7th edition, Mc Graw -Hill, New York, 1978.
31. Denton, J. D.; Cumpsty, N. A. Loss mechanisms in turbomachines. I. Mech E paper C260/87, 1987.
32. Boyer, K. M.; O'Brien, W. F. An Improved Streamline Curvature Approach for Off-Design Analysis of Transonic Axial Compression Systems. *ASME J. Turbomach.*, **2003,** 125(3), 475–481.
33. Yang, X. H. Integrative Design Method of Multi-Configuration Compression System and Aerodynamic Investigation of two Counter-Rotating Fan Types. Ph.D. thesis, Beijing University of Aeronautics and Astronautics, Beijing, China, 2011.
34. Yang, X. H.; Shan, P. Design of Two Counter-rotating Fan Types and CFD Investigation of Their Aerodynamic Characteristics. ASME Paper No. GT2011-45426, 2011.